PAPER

Check for updates

A MOF-derived self-template strategy toward cobalt phosphide electrodes with ultralong cycle life and high capacity†

Guoliang Xia, [ID][a] Jianwei Su,[a] Mengsi Li,[a] Peng Jiang, [ID][a] Yang Yang[a] and Qianwang Chen*[ab]

Phosphides have high theoretical capacity and low redox voltage, and thus could be favorable for lithium storage. Still, huge volume changes and low electroconductivity hinder their application as the anode materials in lithium-ion batteries. Here, cobalt phosphide nanoparticles encapsulated in a nitrogen-doped carbon matrix by using metal–organic frameworks (ZIF-67) as a self-template have been successfully synthesized and showed excellent electrochemical performance as an anode material for lithium-ion batteries. Cobalt-phosphide-based nanohybrids with different phases can be tailored by accurately controlling the pyrolysis temperature. Electrochemical measurements reveal that the electrochemical performance is closely related to the material phase, and Co_xP-NC-800 nanohybrids with two phases exhibit an ultralong cycle life of 1800 cycles at a current density of 1 A g^{-1}. And a high reversible specific capacity of 1224 mA h g^{-1} could be delivered after 100 cycles at a current density of 0.1 A g^{-1}.

Introduction

As one of the most important electrochemical energy-storage devices, lithium-ion batteries currently provide the dominant power sources for a range of devices, including portable electronic devices and electric vehicles in view of high energy density and long lifespan.[1] However, as an anode material in LIBs, commercial graphite has a limited theoretical capacity of around 372 mA h g^{-1}, which is far from the requirements for high capacity. Thus, it is of great importance to search for advanced electrode materials in terms of high capacity, long cycle life, and superior rate capacity. Beyond intercalation-based electrodes like graphite electrodes, electrodes based on conversion reaction mechanisms, such as oxides, sulfides, and phosphides, display more promising capacity and lifespan for lithium storage.[2–5] Compared to oxides or sulfides, transition metal phosphides have a lower and hence more favorable potential for lithium storage.[6] However, little attention has been paid to the phosphides as a result of complicated synthesis. The synthesis of most reported is carried out at high temperatures in boiling organic

solvents or through reactions between a phosphorus source and the precursor, which are placed at separated sites in a combustion boat.[7] Therefore, facile and large-scale ways are pursued.

Although phosphides have high theoretical capacity and low redox voltage, a dramatic volume variation occurs during cycling like most of the metal oxides, which results in pulverization, aggregation, and loss of contact between the active material and the current collector.[8] On the other hand, the low intrinsic electrical conductivity hinders fast chemical diffusion in the electrode. To solve these problems, decreasing the phosphides to the nanoscale or coating carbon layers proves to be effective as a result of larger electrode–electrolyte contact areas, shorter diffusion paths for both electronic and ionic transfer, and buffer environment.[9]

Metal–organic frameworks (MOFs), with tunable pore sizes, large accessible specific surface areas and skeletal structures, are regarded as promising porous crystalline materials with potential applications in gas adsorption and separation,[10] catalysis,[11–14] and electrochemical energy storage and conversion.[15–17] Especially, MOFs have been widely used as a template or precursor to synthesize metal oxides applied in energy storage and conversion.[2,18–20] Zeolitic Imidazolate Frameworks (ZIFs), a typical MOF, fabricated by metal ions coordinated with imidazole ligands, are rich in nitrogen, carbon, and metal ions.[21] Therefore, ZIFs could behave as an ideal precursor for nitrogen-doped carbon, metal oxides, and metal embedded in nitrogen-doped carbon. For instance, using ZIF-8 as a precursor, Zheng *et al.* reported nitrogen-doped graphene particle analogues, which exhibit excellent performance as an

[a]Hefei National Laboratory for Physical Science at Microscale, Department of Materials Science & Engineering, Collaborative Innovation Center of Suzhou Nano Science and Technology, University of Science and Technology of China, Hefei 230026, China

[b]High Magnetic Field Laboratory, Hefei Institutes of Physical Science, Chinese Academy of Sciences, Hefei 230031, China. E-mail: cqw@ustc.edu.cn

This journal is © The Royal Society of Chemistry 2017

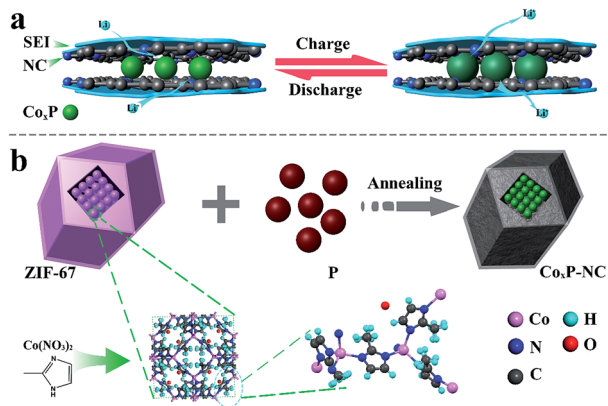*J. Mater. Chem. A*, 2017, 5, 10321–10327 | 10321

Fig. 1 (a) Schematic illustration of the proposed buffer environment provided by a carbon matrix during the charge–discharge process. (b) Schematic illustration of the formation of Co$_x$P-NC polyhedra.

anode for lithium-ion batteries.[22] Highly symmetric porous Co$_3$O$_4$ hollow dodecahedra with nanometer-sized building blocks have been synthesized by Wu *et al.*, which show high lithium storage capacities and excellent cycling performance as anode materials for lithium-ion batteries.[23] Based on a pyrolysis process of predesigned bimetallic Zn/Co zeolitic imidazolate framework, Yin *et al.* reported a new strategy for achieving stable Co single atoms on nitrogen-doped porous carbon with high metal loading over 4 wt%.[24] Starting with ZIF-67 particles as a single precursor, Xia *et al.* synthesized a hollow framework, constructed from interconnected crystalline NCNTs, as an efficient and stable bifunctional electrocatalyst for the ORR and the OER.[25] As we mentioned above, metal phosphides could be a favorable electrode material, while MOF-based metal phosphides are widely investigated in respect of catalysis,[14,26] not yet in lithium storage. Here, we present a convenient and MOF-derived self-template strategy for the synthesis of cobalt phosphide nanoparticles embedded in the polyhedral porous nitrogen-doped carbon (denoted as Co$_x$P-NC). Through the *in situ* synthesis and enclosed carburization reaction, cobalt phosphide nanoparticles are homogeneously distributed in a carbon network, which not only provides efficient pathways for electrons and ions, but also offers sufficient void space to accommodate the volume expansion during cycling, as shown in Fig. 1a. Therefore, high reversible capacity, rate capability, and long cycling life were achieved.

Materials and methods

Material preparation

All chemicals are of analytical grade, and were used without any further purification. The ZIF-67 precursor was synthesized according to a previous report. The typical experiment was carried out as follows: solution A: 1 mmol cobaltous nitrate hexahydrate was dissolved in a methyl alcohol (25 ml) system under agitated stirring for nearly 5 minutes to get a transparent solution. Solution B: 4 mmol 2-methylimidazole (MeIM) was dissolved in 25 ml of methyl alcohol. After shaking solution B for several minutes, solution B was poured into solution A with

continuing stirring and the color of solution A was changed from pink to deep purple immediately. After stirring for nearly 10 minutes, the whole solution was placed undisturbed for 24 hours. The resulting precipitates were collected by centrifugation, thoroughly washed with methyl alcohol several times and finally dried in an oven at 60 °C.

In a typical synthesis of Co$_x$P-NC hybrid composites, 100 mg ZIF-67 and 50 mg red phosphorus were mixed with the help of a mortar. Then the mixture was heated to desired temperatures (700–900 °C) at a rate of 2 °C min^{-1} and maintained for 2 hours under nitrogen atmosphere to produce Co$_x$P-NC-T (T is the pyrolysis temperature).

Material characterization

The power X-ray diffraction (XRD) patterns of all samples were recorded with an X-ray diffractometer (Japan Rigaku D/MAX-γA) equipped with Cu-Kα radiation ($\lambda = 1.54178$ Å) over a 2θ range of 20–80°. Field emission scanning electron microscopy (FE-SEM) images were collected on a JEOL JSM-6700 M scanning electron microscope. Transmission electron microscope (TEM) images were taken on a Hitachi H-800 transmission electron microscope using an accelerating voltage of 200 kV, and a high-resolution transmission electron microscope (HRTEM) (jeol-2011) was operated at an acceleration voltage of 200 kV. The specific surface area was evaluated at 77 K (Micromeritics ASAP 2020) using the Brunauer–Emmett–Teller (BET) method, while the pore volume and pore size were calculated according to the Barrett–Joyner–Halenda (BJH) formula applied to the adsorption branch. Thermogravimetric analysis (TGA) was carried out using a Shimzdzu-50 thermoanalyser under nitrogen flow. XPS measurements were performed on a VGESCALAB MKIIX-ray photoelectron spectrometer with an Mgk$_\alpha$ excitation source (1253.6 eV).

Electrochemical measurements

The electrochemical behavior of Co$_x$P-NC-T was studied using CR2032 coin-type cells with lithium serving as the counter electrode and the reference electrode. To prepare a working electrode, the as-synthesized active material (Co$_x$P-NC-T, 50 wt%), conductive material (acetylene black, 30 wt%), and polymer binder (PVDF, 20 wt%) were mixed in N-methyl-2-pyrrolidone. The mixture was subsequently brush-coated on copper foil and then dried at 80 °C for 12 h. The electrolyte used in the cells was 1.00 M LiPF$_6$ in ethylene carbonate and diethyl carbonate (EC/DEC = 1 : 1). The cells were assembled in an argon-filled glovebox with both the moisture and the oxygen content below 1 ppm (Mikrouna, Super (1220/750/900)). Cyclic voltammograms (CV) were obtained on a CHI760E electrochemical workstation. The electrode capacity was measured using the galvanostatic discharge/charge method and employing a battery test system (Neware CT-3008W) with a voltage range between 0.01 and 3.0 V.

Results and discussion

The overall fabrication process for the synthesis of cobalt phosphide polyhedra is described in Fig. 1b. A metal precursor

(cobaltous nitrate hexahydrate) and MeIM linkers were used to assemble ZIF-67 self-templates, which were subsequently mixed thoroughly with red phosphorus in mass ratio. After pyrolysis at a desired temperature under N_2 flow, cobalt phosphides embedded in nitrogen doped carbon can be obtained.

The Co_xP-NC-800 polyhedra with the best performance for lithium storage are used to demonstrate the typical structure characteristics of MOF-derived products Co_xP-NC-T with other similar structures. A filed-emission scanning electron microscopy (FESEM) view of ZIF-67 reveals the formation of uniform polyhedral particles with a submicrometer size of 400–800 nm, which can also be seen from the transmission electron microscopy (TEM) image (Fig. 2a and b). Besides, the XRD pattern of the as-synthesized ZIF-67 well matches with that of simulated ZIF-67, and confirms the phase purity with good crystalline quality (Fig. S1, ESI†). After annealing, the products inherit the polyhedral morphology and uniform size of the precursor ZIF-67 without apparent collapse, as displayed in Fig. 2c and d. The high-resolution TEM (HRTEM) analysis reveals that the lattice fringes with an interspacing distance of 0.22 nm, 0.25 nm, and 0.19 nm corresponded to the (210) planes of orthorhombic Co_2P, (111) and (211) planes of orthorhombic CoP, respectively (Fig. 2e, e-1, e-2 and e-3). Fig. 2f is a TEM graph of annealed Co_xP-NC-800, and it clearly shows that Co_xP-NC-800 polyhedra are composed of numerous small nanoparticles that are uniformly dispersed in the carbon matrix. Such ultrafine cobalt phosphide nanoparticles could be of assistance to highly reduce the solid state diffusion pathway of lithium ions, and the strain caused by their volume change during cycling can be effectively released by the carbon matrix. The elemental mapping reveals the homogeneous distribution of P, Co, C, N elements in the polyhedral Co_xP-NC-800, as shown in Fig. 2g–k.

The crystallinity and phase information of annealed products were confirmed by X-ray diffraction (XRD) analysis in Fig. 3a. All investigated samples display crystallized structures with distinct characteristic peaks. The cobalt phosphides can be indexed as CoP (PDF #26-0497) and Co_2P (PDF #32-0306). It should be mentioned that different phases could be obtained with the increase of annealing temperature. When the mixture of ZIF-67 and red phosphorus was annealed at 700 °C, only the CoP phase can be detected. While at 800 °C, we observed the appearance of the Co_2P phase and thus the product contains two phases, CoP and Co_2P. At 900 °C, only the pure Co_2P phase is generated. No peaks belonging to metallic cobalt are detected and the signals associated with carbon are barely visible due to its amorphous nature. The graphitization degree of carbon in the synthesized samples can be well characterized by Raman spectra. As shown in Fig. 3b, two peaks at 1354 and 1584 cm^{-1} are observed, which could be attributed to the disordered carbon (D band) and the ordered graphenic carbon (G band), respectively. For the graphitization degree of the carbon, it is generally evaluated according to the ratio of the intensity of the D band to the G band (I_D/I_G). The ratio of intensity between the I_D and I_G band is 1.06/1, indicating the graphenic nature of the nitrogen doped carbon networks with abundant defects.[27]

For the Co_xP-NC-800 sample, the type-IV N2 adsorption–desorption isotherm indicates a mesoporous characteristic (Fig. 3c). The specific surface area calculated using the Brunauer–Emmett–Teller (BET) equation was 326.5 m^2 g^{-1}. The pore size distribution according to the Barrett–Joyner–Halenda (BJH) model reveals that the dominant sizes of the mesopore
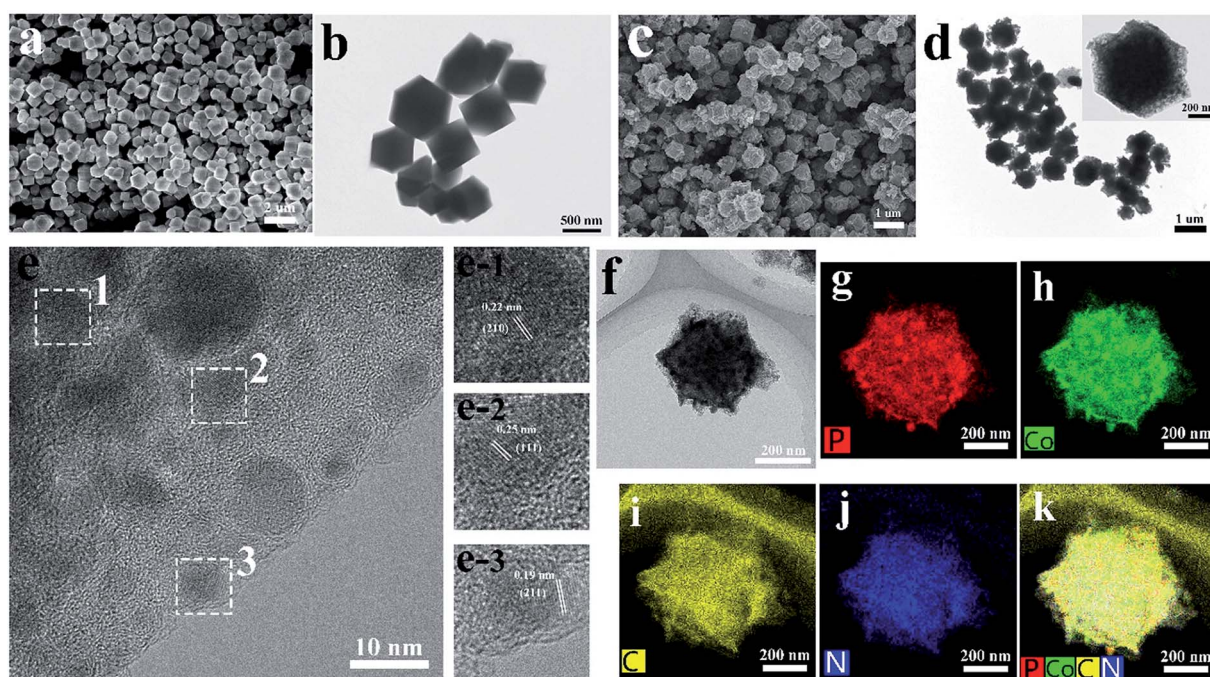

Fig. 2 (a and b) FESEM and TEM images of ZIF-67. (c and d) Typical FESEM and TEM graphs of Co_xP-NC-800. (e and f) HRTEM images of Co_xP-NC-800. (g–k) Corresponding energy-dispersive X-ray spectroscopy (EDX) elemental mapping images of Co_xP-NC-800.
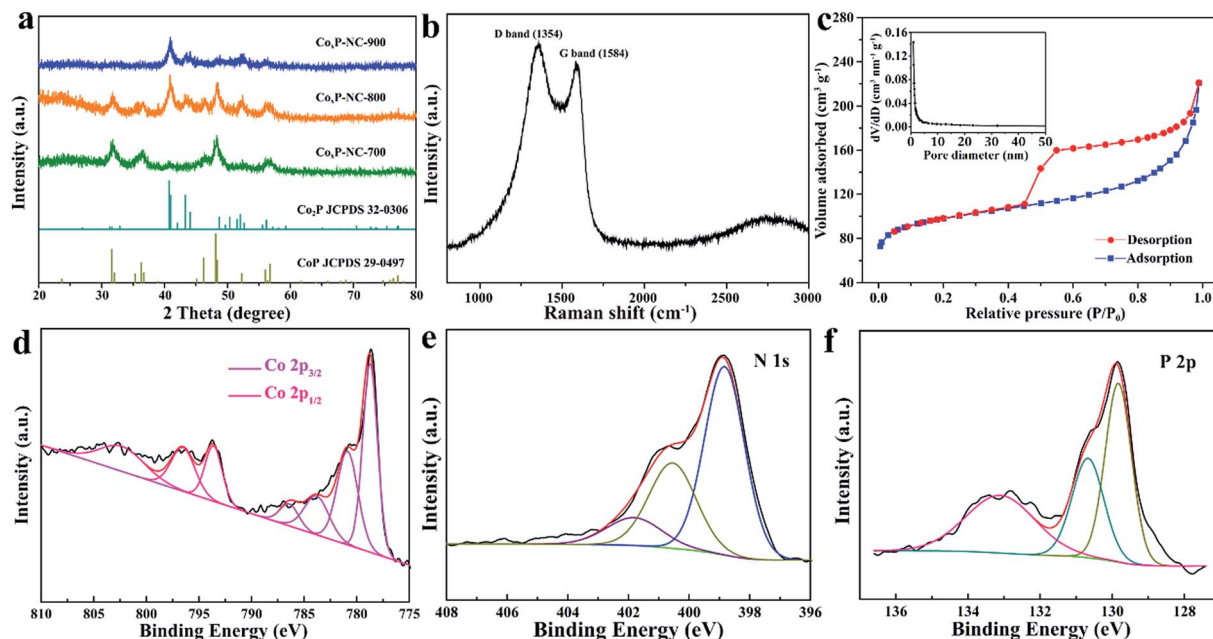
This journal is © The Royal Society of Chemistry 2017

J. Mater. Chem. A, 2017, 5, 10321–10327 | 10323

Fig. 3 (a) XRD patterns of Co$_x$P-NC-700, Co$_x$P-NC-800, and Co$_x$P-NC-900 samples. (b) Raman spectrum of Co$_x$P-NC-800. (c) Nitrogen adsorption/desorption isotherms and pore size distribution of Co$_x$P-NC-800. (d–f) Co 2p, N 1s, and P 2p XPS spectra of the Co$_x$P-NC-800 sample, respectively.

range from 2 to 5 nm. The porous texture should be a result of the decomposition of MeIM, which is favorable for fast accessibility of the inner part of the structure to the electrolyte and ionic diffusion.

The coexistence of Co, P, C, and N elements in Co$_x$P-NC-800 is visualized by a survey scan of X-ray photoelectron spectroscopy (XPS), as shown in Fig. S2 (ESI†). Fig. 3d is the high-resolution Co 2p XPS spectrum. The peaks at 780.9 (2p$_{3/2}$) and 796.5 (2p$_{1/2}$) eV are assigned to the binding energy of Co 2p in CoP,[14] along with two apparent satellite peaks at 802.3 and 786.4 eV, which can be ascribed to the shakeup excitation of the high-spin Co^{2+} ions.[28] In addition, the peaks at 793.6 and 778.7 eV should be assigned to the Co 2p$_{1/2}$ and Co 2p$_{3/2}$ of Co species in Co$_2$P. The higher Co$_{3+}$/Co$_{2+}$ ratio for both Co 2p$_{3/2}$ and Co 2p$_{1/2}$ regions indicates a dominant CoP than Co$_2$P phase. This result also proves the coexistence of CoP and Co$_2$P, which is well consistent with the result of XRD patterns. The N 1s high-resolution spectra display the nitrogen dopants in three types, quaternary N (401.8 eV), pyrrolic N (400.5 eV), and pyridinic N (398.8 eV) (Fig. 3e). Fig. S4 (ESI†) summarizes the fitting results for the N 1s spectrum of the cobalt phosphides, the pyrrolic N and pyridinic N are the dominant N-containing functional groups in the annealed polyhedra. It has been reported that the N-containing species, especially pyrrolic N and pyridinic N, can serve as an electrochemically active site for enhancing the capacitive properties.[22] In Fig. 3f, the presence of deconvoluted peaks at 130.6 and 129.8 eV indicates successful phosphidation of cobalt by forming Co$_2$P and CoP,[29] while a peak located at 133.1 eV represents some partially oxidized phosphate species.[30]

As shown in Fig. 4a, the electrochemical route of the Co$_x$-NC-800 electrode toward lithium storage was recorded using cyclic voltammetry (CV) curves at a scan rate of 0.1 mV s^{-1} between 0.0 and 3.0 V for the first three discharge/charge cycles. In the first cycle discharge, the reduction peak locates at around 1.1 V, which is related to the conversion reaction between Co$_2$P/CoP and Li$^+$.[31] The broad peak range from 0 to 1.0 V is due to the irreversible formation reaction of the solid electrolyte interphase (SEI) layer, which almost disappears in the second and third cycles. According to the literature, an observed small peak at 0.6 V, which become wider in the second and third cycle, should also correspond to the reaction of CoP + Li$^+$ + e$^-$ → LiP + Co.[32] The oxidation peaks located at around 1.25 and 2.5 V can be related to the decomposition of Li$_3$P (Li$_3$P → LiP + 2Li$^+$ + 2e$^-$) and SEI, respectively.[33] In the next two cycles, the overlapping curves indicate good reversibility and high coulombic efficiency.

Fig. 4b–d show the representative discharge/charge voltage curves of Co$_x$P-NC-700, Co$_x$P-NC-800, and Co$_x$P-NC-900 within a cutoff window of 0.01–3.0 V at a current density of 0.1 A g^{-1}. The initial discharge and charge capacities were found to be 2680 and 1632 mA h g^{-1} (For Co$_x$P-NC-700), 2450 and 1496 mA h g^{-1} (for Co$_x$P-NC-800), 2093 and 1156 mA h g^{-1} (for Co$_x$P-NC-900), respectively. The corresponding initial capacity losses of 39.2%, 38.9%, and 44.8% are the result of the irreversible process such as the formation of the inorganic solid electrolyte phase film containing LiCO$_3$ and alkyl carbonates and electrolyte decomposition.[34] Even though Co$_x$P-NC-700 exhibits a highest initial discharge capacity, the capacity fade to 820 mA h g^{-1} after 100 cycles. Co$_x$P-NC-800 has highest capacity of 1224 mA h g^{-1} and Co$_x$P-NC-900 also reaches to 1000 mA h g^{-1} at the 100th cycle. Fig. 4e displays the reversible charge/discharge capacity *versus* the cycle number of Co$_x$P-NC-700,
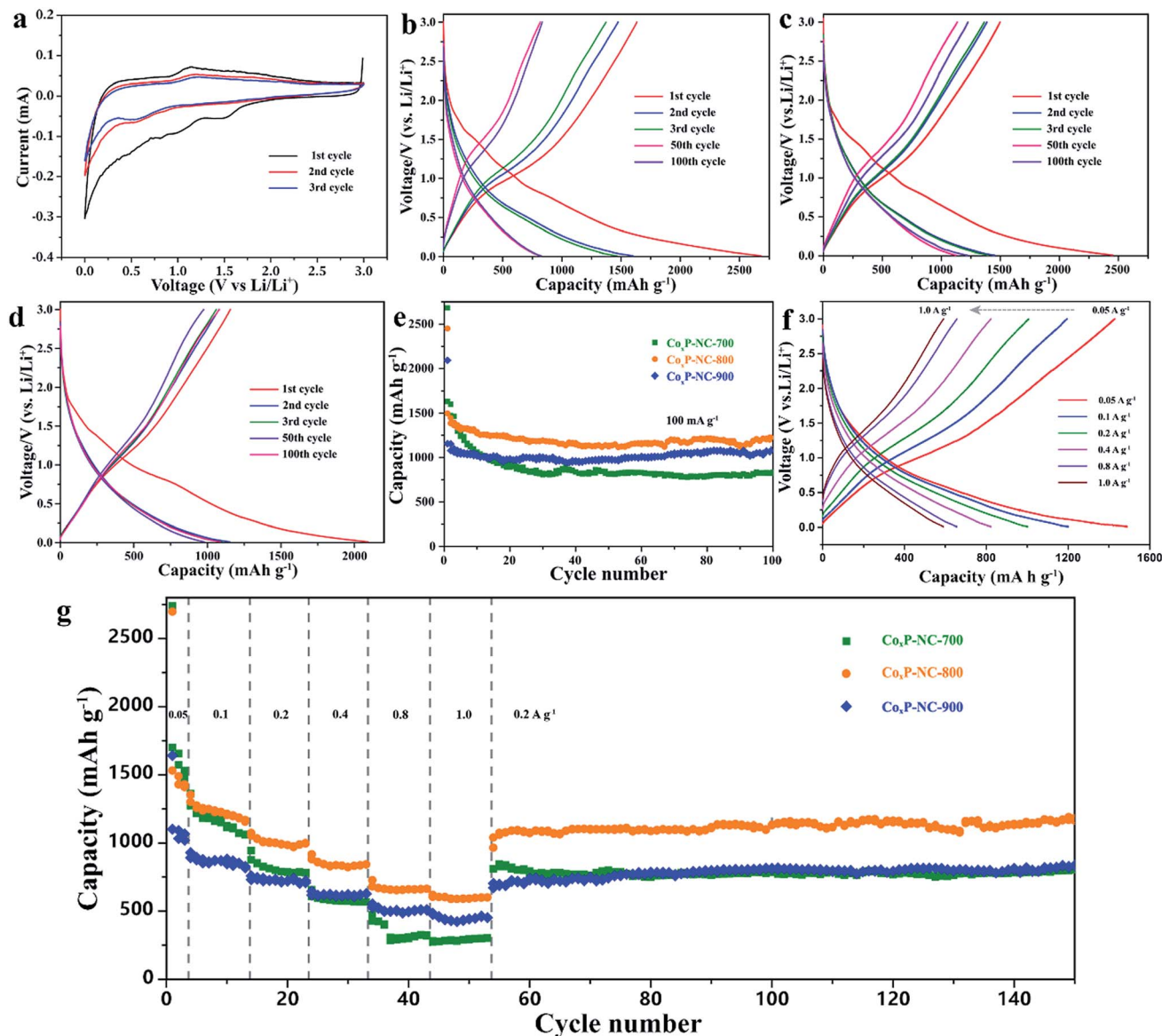
Fig. 4 (a) Cyclic voltammograms of the Co$_x$P-NC-800 sample in a voltage range of 0–3.0 V at a scanning rate of 0.1 mV s^{-1}. (b–d) Discharge–charge voltage profiles of Co$_x$P-NC-700, Co$_x$P-NC-800, and Co$_x$P-NC-900 electrodes for the 1st, 2nd, 3rd, 50th, and 100th cycles. (e) Cycling performance of Co$_x$P-NC-700, Co$_x$P-NC-800, and Co$_x$P-NC-900 electrodes. These tests were conducted at a current density of 0.1 A g^{-1} between 0.01 and 3.0 V. (f) Charge/discharge profiles of the Co$_x$P-NC-800 electrode at different rate current densities and (g) rate performance of the Co$_x$P-NC-700, Co$_x$P-NC-800 and Co$_x$P-NC-900 electrodes at different rate current densities.

Co$_x$P-NC-800, and Co$_x$P-NC-900 at a current density of 0.1 A g^{-1}. After a few cycles, the Co$_x$P-NC-800 electrode shows a stable cycling performance and delivers a high charge capacity of 1224 mA h g^{-1} after 100 cycles. By contrast, the Co$_x$P-NC-700 electrode has a highest initial capacity, but fade quickly to 820 mA h g^{-1} after 30 cycles and subsequently remains stable in the next cycles. The Co$_x$P-NC-900 electrode also displays a stable cycling performance up to 100 cycles, and 1000 mA h g^{-1} was retained. In view of coulombic efficiency (Fig. S5, ESI†), Co$_x$P-NC-800 displays the most stable performance within 100 cycles with a coulombic efficiency near 100% since the fifth cycle. Rate performance is an important criterion for high-power practical applications. The rate performance of Co$_x$P-NC-800 is evaluated

by various current densities, as shown in Fig. 4f. The Co$_x$P-NC-800 electrode delivers the charge capacities of 1420, 1195, 1000, 823, 656, and 590 mA h g^{-1} at the current densities of 0.05, 0.1, 0.2, 0.4, 0.8, and 1.0 A g^{-1}. Moreover, after cycling at high current densities, the capacity returns to 1030 mA h g^{-1} and remains stable for the next cycles, when the current rate abruptly returned to the current density of 0.2 A g^{-1}, showing the superior structural stability of Co$_x$P-NC-700 and Co$_x$P-NC-900 electrodes (Fig. 4g).

Long-term cycling stability is a huge challenge for lithium-ion batteries based on the conversion mechanism. To further demonstrate the advantage of Co$_x$P-NC-T electrodes, a long-term cycling performance at a current density of 1 A g^{-1} for
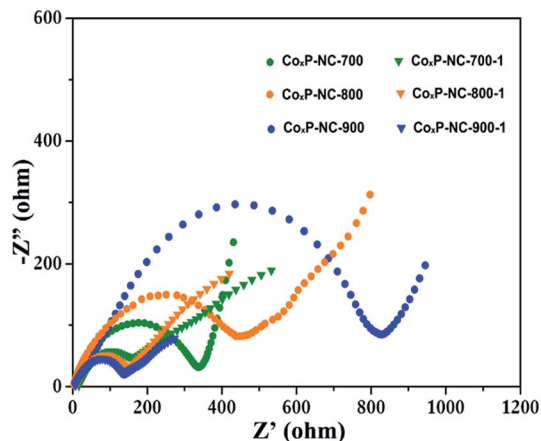
Fig. 5 Electrochemical impedance spectra of the Co$_x$P-NC-700, Co$_x$P-NC-800 and Co$_x$P-NC-900 electrodes before cycling and after cycling at a current density of 1 A g^{-1} (denoted as Co$_x$P-NC-700-1, Co$_x$P-NC-800-1 and Co$_x$P-NC-900-1, respectively).

Co$_x$P-NC-700, Co$_x$P-NC-800, and Co$_x$P-NC-900 electrodes was displayed in Fig. S6 (ESI†). The Co$_x$P-NC-800 electrode exhibits a stable capacity about 550 mA h g^{-1} for 1000 cycles, and could still maintain a capacity of 400 mA h g^{-1} after 1800 cycles. The Co$_x$P-NC-700 electrode shows a changeable capacity, from 300 to 550 (after 1000 cycles) and 390 mA h g^{-1} (after 1600 cycles). The enhanced capacity might be the result of the activation of the active material upon deep cycling, such a similar phenomenon has also been observed in other materials.[35] The Co$_x$P-NC-900 electrode also shows a stable capacity of 440 mA h g^{-1} after 1000 cycles, and maintain 358 mA h g^{-1} after 1255 cycles.

Table S1 (ESI†) summarizes the cycling performance of Co$_x$P-NC-800 and other cobalt phosphide electrode materials.[5,31,36,37] Compared to these reported cobalt phosphide electrode materials and the theoretical capacity of CoP (894 mA h g^{-1}) and Co$_2$P (540 mA h g^{-1}), the Co$_x$P-NC-800 electrode exhibits a better cycling performance and much higher capacity. The remarkable reversibility, rate performance, and long-term cycling stability of the Co$_x$P-NC-800 electrode are based on the unique structure and composition, synergistically combining the advantages of cobalt phosphide nanoparticles and nitrogen-doped carbon.

Although the cobalt phosphide nanoparticles distributed in the carbon skeleton are mechanically isolated, they are electrochemically well connected. For Co$_x$P-NC-700 and Co$_x$P-NC-900 electrodes, both of which have single phase, large capacity with good stability and outstanding rate performance cannot be held at the same time. While for the Co$_x$P-NC-800 electrode, which has two phases, it can display the two advantages together and shows superiority, which indicates that phases may become an important factor affecting the Li-storage properties. Besides, the density functional theoretical calculation suggested that Co$_2$P has better stability with the orthorhombic structure than with the hexagonal structure and the stability of Co–P compounds will decrease with the increase in the P element content.[38] The porous nitrogen-doped carbon matrix not only prevents the aggregation of the active nanoparticles,

but also improves electrochemical conductivity and provides active sites for lithium storage.[39] The internal void space can accommodate the volume change of active nanoparticles to maintain carbon network integration for long-term cycling, thus resulting in a stable cycling performance. The SEM graphs of the Co$_x$P-NC-800 electrode after cycling are shown in Fig. S7.† It is clearly shown that the polyhedral morphology could be well retained, which proves the superior structure stability of the Co$_x$P-NC-800 electrode. And such a feature also endows the current Co$_x$P-NC-800 electrode with good rate performance and cycling stability.

In order to further understand the remarkable cycling stability, electrochemical impedance spectroscopy (EIS) is applied to investigate the conductivity change of the as-prepared electrodes before cycling and after 1000 cycles at 1 A g^{-1} (Fig. 5). In particular, the semicircle located in the medium frequency region in the Nyquist plots is associated with the internal resistances of the electrodes.[37] The Co$_x$P-NC-T electrodes before cycling show an increased impedance with temperature increasing. However, after 1000 cycles at 1 A g^{-1}, all electrodes exhibit nearly overlapped small semicircles, which displays observable impedance decrease. This phenomenon indicates that the Co$_x$P-NC-T electrodes maintain good electron-transport during the cycling process. Besides, the small resistances also agreed well with the excellent long-term cycling performances (Fig. S6†).

Conclusion

In summary, a MOF-derived self-template strategy has been developed to facilely synthesize Co$_x$P-NC hybrids with tunable compositions. The *in situ* generated carbon matrix provides a porous network with Co$_x$P nanoparticles homogeneously embedded in the nitrogen-doped carbon matrix. As a result, Co$_x$P-NC-T nanohybrids show an excellent electrochemical performance when they are evaluated as the anode material for lithium-ion batteries. Especially, the Co$_x$P-NC-800 electrode combining two phases of Co$_2$P and CoP, exhibits a high capacity of 1224 mA h g^{-1} after 100 cycles at a current density of 0.1 A g^{-1}, and an ultralong cycle life of 1800 cycles at a current density of 1 A g^{-1}. Moreover, the MOF-derived self-template method is facile and scalable, and can be a general route for designing and fabricating other metal phosphides for lithium storage or catalysis.

Acknowledgements

Notes and references

1 Y. Tang, Y. Zhang, W. Li, B. Ma and X. Chen, *Chem. Soc. Rev.*, 2015, **44**, 5926–5940.

2 L. Hu, N. Yan, Q. Chen, P. Zhang, H. Zhong, X. Zheng, Y. Li and X. Hu, *Chem.–Eur. J.*, 2012, **18**, 8971–8977.

3 J. Zhang, L. Yu and X. W. D. Lou, *Nano Res.*, 2017, **11**, 1–7.

4 L. Yu, J. F. Yang and X. W. Lou, *Angew. Chem., Int. Ed.*, 2016, **55**, 13422–13426.

5 J. Yang, Y. Zhang, C. Sun, H. Liu, L. Li, W. Si, W. Huang, Q. Yan and X. Dong, *Nano Res.*, 2016, **9**, 612–621.

6 C. Wu, P. Kopold, P. A. van Aken, J. Maier and Y. Yu, *Adv. Mater.*, 2017, **29**, 160415.

7 S. Carenco, D. Portehault, C. Boissière, N. Mézailles and C. Sanchez, *Chem. Rev.*, 2013, **113**, 7981–8065.

8 M. V. Reddy, G. V. Subba Rao and B. V. R. Chowdari, *Chem. Rev.*, 2013, **113**, 5364–5457.

9 X. Wang, H.-M. Kim, Y. Xiao and Y.-K. Sun, *J. Mater. Chem. A*, 2016, **4**, 14915–14931.

10 J.-R. Li, R. J. Kuppler and H.-C. Zhou, *Chem. Soc. Rev.*, 2009, **38**, 1477–1504.

11 Y. Yang, Z. Lun, G. Xia, F. Zheng, M. He and Q. Chen, *Energy Environ. Sci.*, 2015, **8**, 3563–3571.

12 D. P. Kumar, J. Choi, S. Hong, D. A. Reddy, S. Lee and T. K. Kim, *ACS Sustainable Chem. Eng.*, 2016, **4**, 7158–7166.

13 X.-Y. Yu, Y. Feng, B. Guan, X. W. Lou and U. Paik, *Energy Environ. Sci.*, 2016, **9**, 1246–1250.

14 R. Wu, D. P. Wang, K. Zhou, N. Srikanth, J. Wei and Z. Chen, *J. Mater. Chem. A*, 2016, **4**, 13742–13745.

15 W. Xia, A. Mahmood, R. Zou and Q. Xu, *Energy Environ. Sci.*, 2015, **8**, 1837–1866.

16 L. Hu and Q. Chen, *Nanoscale*, 2014, **6**, 1236–1257.

17 L. Zhang, H. B. Wu, S. Madhavi, H. H. Hng and X. W. Lou, *J. Am. Chem. Soc.*, 2012, **134**, 17388–17391.

18 F. Zheng, G. Xia, Y. Yang and Q. Chen, *Nanoscale*, 2015, **7**, 9637–9645.

19 L. Zhang, H. B. Wu and X. W. Lou, *J. Am. Chem. Soc.*, 2013, **135**, 10664–10672.

20 N. Yan, L. Hu, Y. Li, Y. Wang, H. Zhong, X. Hu, X. Kong and Q. Chen, *J. Phys. Chem. C*, 2012, **116**, 7227–7235.

21 J. C. Tan, T. D. Bennett and A. K. Cheetham, *Proc. Natl. Acad. Sci. U. S. A.*, 2010, **107**, 9938–9943.

22 F. Zheng, Y. Yang and Q. Chen, *Nat. Commun.*, 2014, **5**, 5261.

23 R. Wu, X. Qian, X. Rui, H. Liu, B. Yadian, K. Zhou, J. Wei, Q. Yan, X.-Q. Feng, Y. Long, L. Wang and Y. Huang, *Small*, 2014, **10**, 1932–1938.

24 P. Yin, T. Yao, Y. Wu, L. Zheng, Y. Lin, W. Liu, H. Ju, J. Zhu, X. Hong, Z. Deng, G. Zhou, S. Wei and Y. Li, *Angew. Chem., Int. Ed.*, 2016, **55**, 10800–10805.

25 B. Y. Xia, Y. Yan, N. Li, H. B. Wu, X. W. Lou and X. Wang, *Nat. Energy*, 2016, **1**, 15006.

26 P. He, X.-Y. Yu and X. W. Lou, *Angew. Chem., Int. Ed.*, 2017, **129**, 3955–3958.

27 B. Kong, L. Zu, C. Peng, Y. Zhang, W. Zhang, J. Tang, C. Selomulya, L. Zhang, H. Chen, Y. Wang, Y. Liu, H. He, J. Wei, X. Lin, W. Luo, J. Yang, Z. Zhao, Y. Liu, J. Yang and D. Zhao, *J. Am. Chem. Soc.*, 2016, **138**, 16533–16541.

28 Y.-P. Zhu, Y.-P. Liu, T.-Z. Ren and Z.-Y. Yuan, *Adv. Funct. Mater.*, 2015, **25**, 7337–7347.

29 J. Song, C. Zhu, B. Z. Xu, S. Fu, M. H. Engelhard, R. Ye, D. Du, S. P. Beckman and Y. Lin, *Adv. Energy Mater.*, 2017, **7**, 1601555.

30 P. E. R. Blanchard, A. P. Grosvenor, R. G. Cavell and A. Mar, *Chem. Mater.*, 2008, **20**, 7081–7088.

31 D. Yang, J. Zhu, X. Rui, H. Tan, R. Cai, H. E. Hoster, D. Y. W. Yu, H. H. Hng and Q. Yan, *ACS Appl. Mater. Interfaces*, 2013, **5**, 1093–1099.

32 Z. Zhang, J. Yang, Y. Nuli, B. Wang and J. Xu, *Solid State Ionics*, 2005, **176**, 693–697.

33 M. C. López, G. F. Ortiz and J. L. Tirado, *J. Electrochem. Soc.*, 2012, **159**, A1253–A1261.

34 M. V. Reddy, T. Yu, C. H. Sow, Z. X. Shen, C. T. Lim, G. V. Subba Rao and B. V. R. Chowdari, *Adv. Funct. Mater.*, 2007, **17**, 2792–2799.

35 S. Niu, Z. Wang, T. Zhou, M. Yu, M. Yu and J. Qiu, *Adv. Funct. Mater.*, 2017, **27**, 1605332.

36 A. Lu, X. Zhang, Y. Chen, Q. Xie, Q. Qi, Y. Ma and D.-L. Peng, *J. Power Sources*, 2015, **295**, 329–335.

37 J. Jiang, C. Wang, W. Li and Q. Yang, *J. Mater. Chem. A*, 2015, **3**, 23345–23351.

38 Z. Yang, L. Liu, X. Wang, S. Yang and X. Su, *J. Alloys Compd.*, 2011, **509**, 165–171.

39 L. Qie, W.-M. Chen, Z.-H. Wang, Q.-G. Shao, X. Li, L.-X. Yuan, X.-L. Hu, W.-X. Zhang and Y.-H. Huang, *Adv. Mater.*, 2012, **24**, 2047–2050.

This journal is © The Royal Society of Chemistry 2017

J. Mater. Chem. A, 2017, **5**, 10321–10327 | **10327**